

Article

Open Access



Understanding of working mechanism of lithium difluoro(oxalato) borate in Li||NCM85 battery with enhanced cyclic stability

Xuerui Yang^{1,2,#}, Yaxin Huang^{1,#}, Jianhui Li³, Weilin Huang¹, Wen Yang⁴, Changquan Wu², Shijun Tang⁵, Fucheng Ren⁵, Zhengliang Gong^{5,*}, Naigen Zhou^{2,*}, Yong Yang^{1,5,*}

¹College of Chemistry and Chemical Engineering & Tan Kah Kee Innovation Laboratory (IKKEM), Xiamen University, Xiamen 361102, Fujian, China.

²School of Physics and Materials Science, Nanchang University, Nanchang 330031, Jiangxi, China.

³School of Chemistry, South China Normal University, Guangzhou 510006, Guangdong, China.

⁴College of Chemistry and Chemical Engineering, Jiangxi Province Engineering Research Center of Ecological Chemical Industry, Jiujiang University, Jiujiang 332005, Jiangxi, China.

⁵School of Energy, Xiamen University, Xiamen 361102, Fujian, China.

#Authors contributed equally.

***Correspondence to:** Prof. Zhengliang Gong, School of Energy, Xiamen University, Xiamen 361102, Fujian, China. E-mail: zlgong@xmu.edu.cn; Prof. Naigen Zhou, School of Physics and Materials Science, Nanchang University, Nanchang 330031, Jiangxi, China. E-mail: ngzhou@ncu.edu.cn; Prof. Yong Yang, State Key Laboratory of Physical Chemistry of Solid Surfaces, Department of Chemistry and College of Chemistry and Chemical Engineering & Tan Kah Kee Innovation Laboratory (IKKEM), Xiamen University, Xiamen 361102, Fujian, China. E-mail: yyang@xmu.edu.cn

How to cite this article: Yang X, Huang Y, Li J, Huang W, Yang W, Wu C, Tang S, Ren F, Gong Z, Zhou N, Yang Y. Understanding of working mechanism of lithium difluoro(oxalato) borate in Li||NCM85 battery with enhanced cyclic stability. *Energy Mater* 2023;3:300029. <https://dx.doi.org/10.20517/energymater.2023.10>

Received: 15 Feb 2023 **First Decision:** 12 Apr 2023 **Revised:** 10 May 2023 **Accepted:** 1 Jun 2023 **Published:** 3 Jul 2023

Academic Editors: Elie Paillard, Xiongwei Wu **Copy Editor:** Fangling Lan **Production Editor:** Fangling Lan

Abstract

Despite the significant advances achieved in recent years, the development of efficient electrolyte additives to mitigate the performance degradation during long-term cycling of high-energy density lithium||nickel-rich (Li||Ni-rich) batteries remains a significant challenge. To achieve a rational design of electrolytes and avoid unnecessary waste of resources due to trial and error, it is crucial to have a comprehensive understanding of the underlying mechanism of key electrolyte components, including salts, solvents, and additives. Herein, we present the utilization of lithium difluoro(oxalato) borate (B) (LiDFOB), a B-containing lithium salt, as a functional additive for Li||LiNi_{0.85}Co_{0.1}Mn_{0.05}O₂ (NCM85) batteries, and comprehensively investigate its mechanism of action towards enhancing the stability of both anode and cathode interfaces. The preferential reduction and oxidation decomposition of DFOB leads to the formation of a robust and highly electronically insulating boron-rich interfacial



© The Author(s) 2023. **Open Access** This article is licensed under a Creative Commons Attribution 4.0 International License (<https://creativecommons.org/licenses/by/4.0/>), which permits unrestricted use, sharing, adaptation, distribution and reproduction in any medium or format, for any purpose, even commercially, as long as you give appropriate credit to the original author(s) and the source, provide a link to the Creative Commons license, and indicate if changes were made.



film on the surface of both the Li anode and NCM85 cathode. This film effectively suppresses the consumption of active lithium and the severe decomposition of the electrolyte. Furthermore, the presence of B elements in the cathode-electrolyte interfacial film, such as BF_3 , BF_2OH , and BF_2OBF_2 compounds, can coordinate with the lattice oxygen of the cathode, forming strong coordination bonds. This can significantly alleviate lattice oxygen loss and mitigate detrimental structural degradation of the Ni-rich cathode. Consequently, the Li||NCM85 battery cycled in LiDFOB-containing electrolyte displays superior capacity retention of 74% after 300 cycles, even at a high charge cut-off voltage of 4.6 V. The comprehensive analysis of the working mechanisms of LiDFOB offers valuable insights for the rational design of electrolytes featuring multifunctional lithium salts or additives for high energy density lithium metal batteries.

Keywords: Lithium metal battery, lithium difluoro(oxalate) borate, Li anode, Ni-rich cathode, SEI/CEI film

INTRODUCTION

Lithium-ion batteries (LIBs) are widely used in various electronic equipment as energy storage devices, while the rapid development of electric vehicles (EVs) has put forward higher requirements for LIBs in terms of energy/power density and cyclic stability^[1-6]. To this end, the development of high-specific energy LIBs with lithium metal as the anode (currently the largest energy density) and a suitable cathode is the key to improving the overall energy density of LIBs^[7-10]. Among all the identified cathode materials, nickel (Ni)-rich-layered oxide $\text{Li}[\text{Ni}_x\text{Co}_y\text{Mn}_{1-x-y}]\text{O}_2$ ($x \geq 0.8$) with suitable Ni, Co, and Mn atomic ratios is considered one of the most promising cathode materials due to their high specific capacity of more than 200 mAh g⁻¹ and low cost^[11,12]. However, the practical application of the Ni-rich cathode material is limited by severe capacity decay and thermal instability^[13]. Several possible reasons have been proposed to explain the performance degradation of Ni-rich materials, mainly including irreversible structural changes and interfacial degradation^[14]. On the one hand, at a highly delithiated state, the irreversible phase transition from the second hexagonal phase (H2) to the third hexagonal phase (H3), accompanied by abrupt lattice contraction and rise of internal stress, will result in partial structure collapse at the near-surface area of crystal and serious grain intergranular or intragranular cracking of particles^[15,16]. Meanwhile, the structure collapse accompanied by oxygen evolution and transition metal dissolution will cause the spread of this collapse and cracks into the particle core, which leads to fast capacity loss. Additionally, the electrolyte can penetrate into these cracks, which can be catalyzed by highly active Ni^{4+} and superoxide ions (O^-) to form an undesired phase transition layer and excessive deposition of electrolyte decomposition products. This results in a substantial reduction in the kinetics of Li-ion (Li^+) migration and electron transfer of the electrode^[17-19]. In addition, Ni^{4+} ions are easily reduced into stable Ni^{2+} ions in the presence of O^- , resulting in capacity loss and O_2 release^[20]. Meanwhile, due to the similar size of Ni^{2+} and Li^+ , it will cause more serious $\text{Li}^+/\text{Ni}^{2+}$ mixing, which further reduces the stability of the structure^[21,22]. Therefore, achieving a stable Ni-rich cathode necessitates the high stability of surficial/interfacial structure, especially at a higher voltage.

To solve these problems, several strategies have been explored in recent studies, such as coherent surface coating^[20,23-30] and near-surface element doping or substitution^[31-37], to better stabilize the near-surface structure of the material (especially the stability of surface lattice oxygen) and effectively suppress electrolyte decomposition. However, these approaches usually involve complicated synthetic processes, and the introduction of inert compositions reduces the specific capacity of cathodes. More importantly, these methods can only target the cathode alone but cannot simultaneously protect the anode, especially the hyperactive lithium metal anode. Detrimental and persistent interfacial side reactions occur between lithium metal and the electrolyte, which induces the generation of lithium dendrites and inactive lithium, resulting in short cycle life and causing safety issues^[38-42].

In this regard, optimizing electrolytes by using interfacial film-formation functional additives to simultaneously regulate Ni-rich cathode and Li anode interfacial properties is a promising strategy^[43,44]. Among the diverse electrolyte additives that have been reported so far, borate (B)-containing additives, especially B-containing lithium salts, have been employed as effective salts or additives for high-voltage cathodes or alkali metal anodes^[45-60]. For example, Zhang *et al.* introduced trace (~2%) lithium bis(oxalato)borate (LiBOB) as an electrolyte additive to improve the cyclic stability of Li-rich layered oxide (LRLO) cathode by optimizing the cathode interfacial structure and eliminating the detrimental nucleophilic superoxide attack under the synergy effect of LiPF₆^[61]. Chen *et al.* demonstrated lithium difluorobis(oxalato)phosphate (LiDFBOP) as the multifunctional additive can build a stable and robust organic/inorganic hybrid interphase on Na anode and Na₃V₂(PO₄)₂F₃ cathode surface by the preferential reduction and oxidation of DFBO, realizing excellent cyclic stability for high-voltage Na||Na₃V₂(PO₄)₂F₃ system^[62]. Mao *et al.* configured 1 M lithium difluoro(oxalate) borate (LiDFOB)-based electrolyte, where the LiDFOB can not only *in-situ* construct a hierarchical and robust cathode/electrolyte interface (CEI) film on the LiNi_{0.8}Co_{0.1}Mn_{0.1}O₂ (NCM811) cathode surface but also induce the uniform plating of Li, resulting in greatly improved cyclic stability of Li||NCM811 batteries^[63]. While B-containing lithium salts are widely utilized in batteries, a systematic investigation of the differences in the interfacial films formed from their decomposition on the anodes and cathodes is rarely reported. It is crucial to have a comprehensive understanding of the working mechanism of key components in the electrolyte for the rational design of electrolytes to improve the performance and stability of the batteries.

Herein, LiDFOB, as a B-containing lithium salt type additive incorporating the advantages of both lithium tetrafluoroborate (LiBF₄) and LiBOB, was selected for high-energy-density Li||LiNi_{0.85}Co_{0.1}Mn_{0.05}O₂ (NCM85) battery. Theoretical calculations and experimental studies systematically demonstrated that DFOB⁻ is preferentially reduced on the Li anode surface to form a highly electrochemically stable, electronically insulating, and ion-conductive solid electrolyte interface (SEI) film under the synergistic effect of ethylene carbonate (EC), which effectively promotes the homogenous plating of Li and suppresses the continuous decomposition of the electrolyte and the formation of inactive lithium. On the NCM85 cathode surface, the DFOB⁻ is preferentially oxidized and spontaneously captures the harmful hydrofluoric acid (HF) and O⁻ to form an antioxidant and electronically insulating CEI film, which can effectively suppress the oxidative decomposition of the electrolyte and the erosion of HF to electrodes. Meanwhile, the B element in CEI film will form a strong bond with the lattice O of the cathode surface, thereby stabilizing the phase structure of NCM85 and inhibiting the subsequent irreversible structural transition and O₂ release. Consequently, the cyclic stability and rate capability of Li||NCM85 batteries are significantly improved, even at a high charge cut-off voltage of 4.6 V. The comprehensive examination of LiDFOB in this work offers valuable insights and helpful guidance for the design of B-containing electrolyte additives or lithium salts for high-energy-density lithium metal batteries.

EXPERIMENTAL

Preparation of electrolytes and electrodes

The electrolytes and electrodes were both prepared in the Mbraun glove box (Ar atmosphere) with moisture and oxygen levels less than 0.1 ppm. 1 M LiPF₆ in EC and ethyl methyl carbonate (EMC) (EC:EMC = 3:7 wt%) (provided by Shenzhen Capchem Technology Co., Ltd.) was used as the base electrolyte. A range of electrolytes was prepared by dissolving various concentrations of LiDFOB (obtained from Guangdong Canrd New Energy Technology Co., Ltd.) additive into the base electrolyte (abbreviated as "base" in the figures). The cathode was prepared by mixing NCM85 (provided by Ningbo Ronbay New Energy Technology Co., Ltd.), polyvinylidene fluoride (mixed in N-methyl-2-pyrrolidone), and acetylene black with the weight ratio of 8:1:1 uniformly. After coating the slurry onto the aluminum current collector (12-mm diameter) and drying in vacuum for 8 h at 110 °C, the cathode was then stored in a glove box for

use. The active material loading of the cathode was $\sim 3 \text{ mg cm}^{-2}$. The electrodes were separated by a single-layer separator (Celgard 2500) in a CR2025 coin cell filled with 100 μL electrolyte.

Electrochemical measurement

The fabricated cells were charged and discharged after standing for 8 h at room temperature, measured by the LAND system (CT2001A, Wuhan, China). For regular cycles, each Li||NCM85 battery was charged/discharged galvanostatically at 0.3 C (1 C = 200 mAh g^{-1}) for two cycles before testing, then set the charge-discharge rate at 1C to analyze cyclability, voltage ranging from 3.0 V to 4.3 V/4.6 V. After two formation cycles at 0.2 C, the rate test was carried out at 1 C, 3 C, 5 C, 7 C, 10 C, and 0.2 C again for five cycles, respectively. A high current charge and discharge test was carried out to further assess the cyclic stability of the batteries at the charge/discharge rate of 2 C/5 C. In the galvanostatic intermittent titration test (GITT), the parameter pulse current was 1 C, the pulse charge/discharge time was 90 s, and the resting time was 2 h. The Li^+ diffusion coefficient is calculated by Equation (1)^[64]:

$$D_{\text{Li}^+} = \frac{4}{\pi\tau} \left(\frac{mV_m}{MS} \right)^2 \left(\frac{\Delta E_s}{\Delta E_t} \right)^2 \quad (1)$$

where D_{Li^+} is the chemical diffusion coefficient, S is the surface area of the electrode (1.13097 cm^2 in our case), τ is pulse duration, ΔE_s is the steady-state voltage change, ΔE_t is the transient voltage change, and m , M , and V_m is the mass, molecular weight (97.28 g mol^{-1}), and molar volume (19.3491 $\text{cm}^3 \text{mol}^{-1}$) of the electrode, respectively. For Li||Li symmetric cells and Li||Cu cells, Li foils with a diameter of 10 mm and 450 μm thickness were used as both working and counter electrodes. Li||Cu cells were performed to evaluate coulombic efficiency (CE) by using Aurbach's test method^[65]. Especially, 4 mAh cm^{-2} of Li was pre-deposited on Cu under a current density of 0.5 mA cm^{-2} and then followed by reversible plating/stripping with 1 mAh cm^{-2} for two cycles, and finally stripping to 1.0 V (vs. Li/Li⁺). This CE was calculated by Equation (2):

$$\text{CE} = (Q_s + Q_c \times n) / (Q_p + Q_c \times n) \quad (2)$$

where Q_s is the final stripping capacity, Q_p is the initial plating capacity, Q_c is the constant plating/stripping capacity for each cycle, and n is the cycle number^[66]. Li||Li symmetric cells were cycled at a current density of 0.5 mA cm^{-2} and a capacity of 1.0 or 3.0 mAh cm^{-2} . Linear sweep voltammetry (LSV) and electrochemical impedance spectrum (EIS) analysis were both performed on an electrochemical workstation (Autolab, PGSTAT-302N, Metrohm, Netherlands), with the sweep scan rate at 1 mV s^{-1} for LSV and a 5 mV amplitude and a frequency between 10^5 Hz and 10 mHz for EIS.

Material characteristic

The batteries were disassembled after cycling, and the electrodes were rinsed and soaked with dimethyl carbonate (DMC) to remove the residual electrolyte and dried naturally in the glove box. Scanning electron microscopy (SEM, Zeiss GeminiSEM 500, Germany) was used to analyze the morphology of Li anodes and NCM85 cathodes. The transmission electron microscope (TEM, JEM-2100HR, Japan) was carried out to analyze the evolution of NCM85 surface microstructure before and after cycling. The ion beam polished with Cross Section Polisher (Leica, EM TIC 3X, Germany) was used to prepare the cross-section samples. The crystal structure and phase transformation of NCM85 were detected by *ex-situ* X-ray diffraction (XRD, Rigaku Ultima IV diffractometer, Japan) and *in-situ* XRD (Bruker D8 discover diffractometer, German) at a scan rate of 5°/min with Cu $K\alpha$ radiation over 2θ range of 20° to 60°. As for the components on the surface of the Li anode and NCM85 cathode, X-ray photoelectron spectroscopy (XPS, Thermo Fisher Scientific, UK) was employed with the binding energy in the measured spectrum calibrated based on C1s at 284.8 eV.

The fitting results of XPS peaks were obtained using XPSPEAK Version 4.0. *In-situ* differential electrochemical mass spectrometry (DEMS) experiments were carried out to test the CO₂ emission during charging using a commercial quadrupole mass spectrometer (Hiden Analytical) equipped with a digital mass flow meter (Bronkhorst). The homemade Swagelok-type cell was assembled in the glove box and then charged to 4.6 V at 0.2 C after resting for 3 h. Time of flight secondary ion mass spectrometry (TOF-SIMS, IONTOF, German) was employed to investigate the surface structure evolution of both NCM85 cathode and Li anode. All detected secondary ions of interest in the TOF-SIMS analysis had a mass resolution of over 17,000. The samples were prepared in a glove box and transferred to the instruments using an air-tight holder during TOF-SIMS characterizations.

Calculation methods

The first-principles calculations were implemented using Vienna Ab-initio Simulation Package (VASP) version 5.4.1^[67] and Gaussian 09 package^[68], with strongly constrained and appropriately normed (SCAN) and Perdew-Burke-Ernzerhof (PBE) functional, respectively. The (104) and (100) surfaces of the layered LiNiO₂ and Cubic lithium metal crystal were simulated by four-layer slab Li₃₂Ni₃₂O₆₄ and Li₁₀₀, respectively. The plane-wave cut-off energy was set to be 520 eV, and the convergence criteria were 10⁻⁴ eV and 0.05 eV Å⁻¹ for electron energy and ions force, respectively, in all calculations. The structures of EC, EMC, LiDFOB, and DFOB⁻ and the corresponding redox reaction process of the EC and DFOB⁻ were optimized at the B3LYP/6-311++G (d, p) level. To investigate the role of the solvent effect, the polarized continuum model (PCM) was performed with a dielectric constant of 20.5 (acetone) as the default solvent^[69]. The atomic charge distributions were analyzed from natural population analysis (NPA) using the natural bond orbital (NBO) theory. The adsorption energy W_{ad} of molecules on the crystal surface can be acquired according to Equation (3):

$$W_{ad} = E_{x-slab} - E_x - E_{slab} \quad (3)$$

where E_{x-slab} , E_x , and E_{slab} are the total energy of the interfacial supercell, the adsorbed redox products, and the bottom layer (LiNiO₂ (104) or Li (100)), respectively. The calculated oxidation potential (E_{ox}) and reduction potential (E_{re}) were converted from the absolute oxidation/reduction potential of the species (vs. Li/Li⁺), according to Equation (4):

$$E_{ox/re} = +/-[G(M^+) - G(M)]/F - 1.4 V \quad (4)$$

where $G(M)$ and $G(M^+)$ are the free energies of the species M and its oxidized/reduced form M^+ at 298.15 K, respectively, and F is the Faraday constant.

RESULTS AND DISCUSSION

Redox activity of LiDFOB

Li/graphite [Figure 1A] and Li/Pt [Figure 1B] cells were assembled to analyze the electrochemical stability of the electrolytes with and without LiDFOB additive, respectively. As shown in Figure 1A, an additional reduction peak at ~1.6 V can be observed before lithiation of graphite in the 2% LiDFOB-containing electrolyte, corresponding to the preferential reduction of LiDFOB compared to the solvent molecules. Besides, a significant negative shift in the onset decomposition potential observed in the LSV curves [Figure 1B] of Li/Pt cell with the LiDFOB-containing electrolyte reveals that LiDFOB is also preferentially oxidized on the cathode surface compared to the base electrolyte. Furthermore, the order of HOMO and LUMO energy levels obtained from the calculations are as follows: DFOB⁻ > LiDFOB > EMC > EC and LiDFOB < DFOB⁻ < EC < EMC, respectively [Figure 1C]. This result further supports the preferential

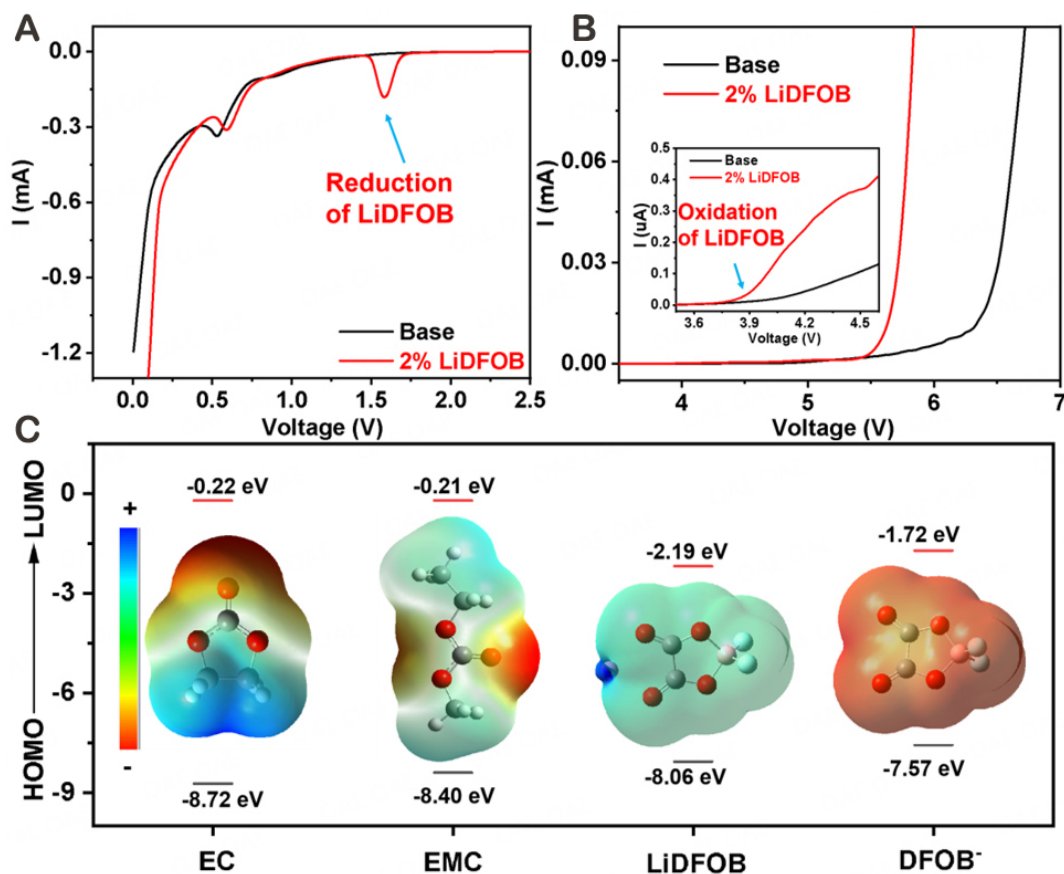


Figure 1. LSV curves of (A) Li/graphite and (B) Li/Pt cells cycled in the electrolytes with & without LiDFOB additive. The inset is the enlarged view within the range of 3.5–4.6 V of (B); (C) Molecular orbital models and calculated HOMO/LUMO energy levels of EC, EMC, Li⁺-DFOB⁻, and DFOB⁻, respectively.

oxidation and reduction of DFOB⁻ and LiDFOB on the cathode and anode surface, which contributes to the formation of the CEI film and SEI film, respectively.

Effects of LiDFOB on Li anode

The effect of the LiDFOB additive on the reversibility of Li plating/stripping was first evaluated using Li||Cu and Li||Li cells. It can be noted from Figure 2A that the CE (evaluated by Aurbach's method^[65]) of the Li||Cu cells increases significantly from 53.95% to 83.82% with the addition of LiDFOB and is accompanied by a decreased nucleation overpotential at a current density of 0.5 mA cm⁻², indicating that LiDFOB-derived SEI film can effectively regulate Li plating/stripping with the lower barrier and enhance the reversibility of active lithium. Besides, the cells with the prelithiated Cu foil deposited with 4.0 mAh cm⁻² Li can stably cycle for more than 60 h in the LiDFOB-containing electrolyte, compared to the sudden voltage fluctuations after cycling for 15 h in the base electrolyte [Supplementary Figure 1]. The voltage fluctuations are related to interfacial instability during the Li plating/stripping process, which results in irreversible loss of active Li in the base electrolyte^[65]. In comparison, the SEI film derived by the addition of LiDFOB is robust to guarantee a stable interface for the homogenous plating/stripping of Li. As a result, the Li||Li symmetric cells with the LiDFOB-containing electrolyte exhibited superior cyclic stability at either 1.0 mAh cm⁻² or the higher plating/stripping capacity of 3.0 mAh cm⁻² [Figure 2B and C]. Then, the morphology of the lithium metal after cycling was studied using SEM. As shown in Figure 2D, a sparse and needle-like morphology on the surface of the cycled Li anode in the base electrolyte is observed. This porous structure with a high surface

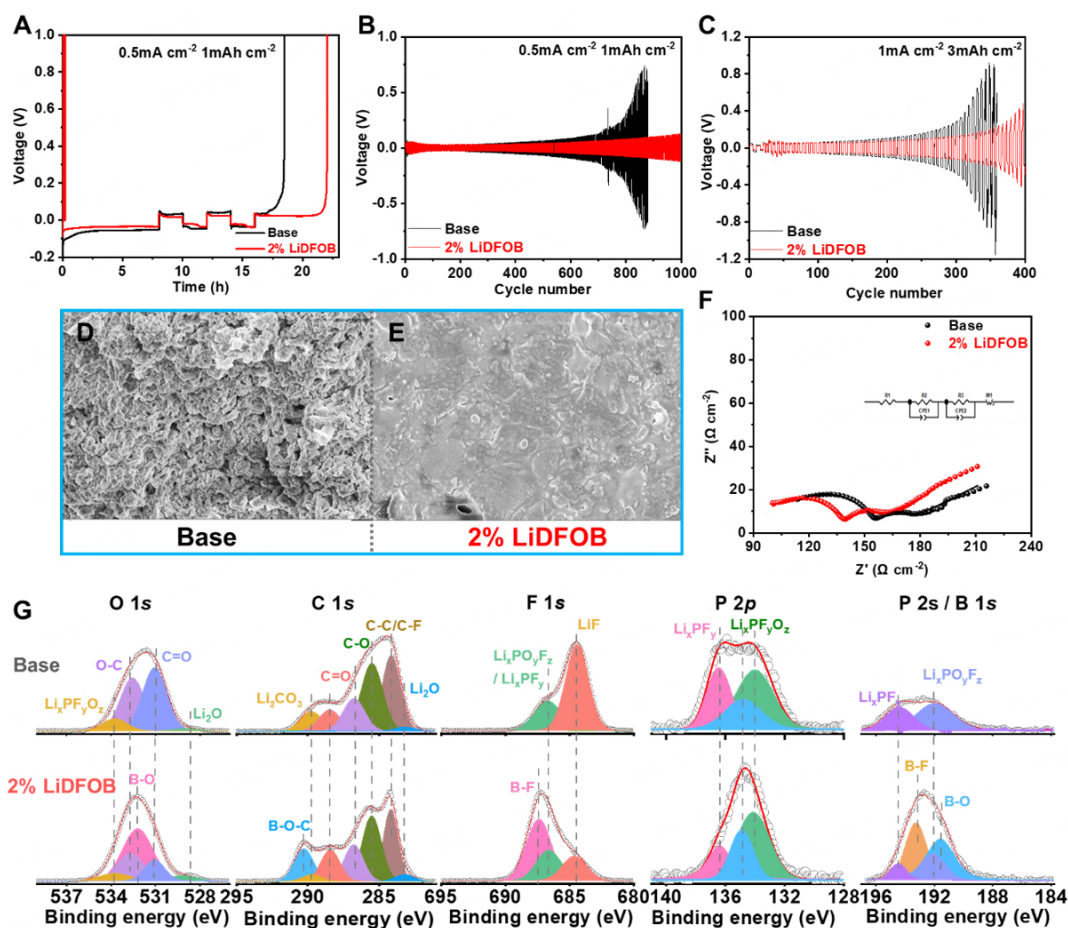


Figure 2. (A) CE in Li||Cu cells by Aurbach's test method with Li stripping/plating at 0.5 mA cm^{-2} and 1 mAh cm^{-2} . The lithium plating/stripping behaviors of Li||Li symmetric cells at (B) 0.5 mA cm^{-2} and 1 mAh cm^{-2} and (C) 1 mA cm^{-2} and 3 mAh cm^{-2} . SEM image of the Li anode after Li plating/stripping at 1 mA cm^{-2} and 3 mAh cm^{-2} in (D) the base electrolyte and (E) LiDFOB-containing electrolytes. (F) Nyquist plots of Li||Li cells after cycling for 400 h at 1 mA cm^{-2} and 3 mAh cm^{-2} in the electrolyte with and without LiDFOB additive. (G) XPS spectra of O 1s, C 1s, F 1s, P 2p, and P 2s/B1s for the cycled Li anode in different electrolytes.

area intensifies the reaction with electrolytes, thus resulting in continuous consumption of electrolytes and active lithium. Differently, a compact and planar structure is presented with the addition of LiDFOB [Figure 2E], further implying that adding LiDFOB can induce the homogeneous plating/stripping of the Li and significantly inhibit the growth of lithium dendrites.

The interfacial impedance of the Li anode after cycling for ~ 400 h at 1 mA cm^{-2} with an areal capacity of 3 mAh cm^{-2} was analyzed by the EIS [Figure 2F], and the corresponding fitting results were listed in Supplementary Table 1. It shows that the ohmic impedance (R_1), interfacial impedance (R_2), and charge transfer impedance (R_3) of cells cycled in the LiDFOB-containing electrolyte are all obviously lower than those in the base electrolyte, indicating the improved interfacial stability. Then, XPS was carried out to explore the interphase components on the cycled lithium metal surface [Figure 2G]. In O 1s spectra, the peaks associated with C-O (285.5 eV) and C=O (288.5 eV) species primarily correspond to ROCO_2Li or polycarbonates resulting from the reaction of Li with organic solvents in the electrolyte. This observation is further supported by the C 1s spectra, which exhibit peaks at 285.5 eV (C-O), 288.5 eV (C=O), and 289.8 eV (Li_2CO_3) [26,70,71]. The intensity of these peaks, represented by the peak areas [Supplementary Figure 2], is significantly lower for the Li anode cycled in the LiDFOB-containing electrolyte than in the base electrolyte,

indicating the effective suppression of electrolyte decomposition by the SEI film derived from LiDFOB. The F 1s spectra provide valuable information regarding the SEI on the Li anode. In the case of the Li anode cycled in the base electrolyte, the observed peaks at 684.42 eV and 686.65 eV can be attributed to the presence of LiF and $\text{LiP}_x\text{F}_y/\text{LiP}_x\text{F}_y\text{O}_z$, resulting from the decomposition of LiPF_6 . It is well known that the decomposition of LiPF_6 to LiF often leads to the generation of PF_5 . While LiF has been extensively studied for its beneficial effects^[72], its advantages may be overshadowed by the strong reactivity of PF_5 with the electrolyte due to its Lewis acid property. Furthermore, [Supplementary Figure 3](#) demonstrates a significantly higher energy barrier for breaking the B-F bond during the reduction decomposition of LiDFOB compared to its ring-opening reaction. This finding suggests that the ring-opening reaction is the predominant pathway for the decomposition of LiDFOB, thereby confirming that a major portion of the LiF originates from the decomposition of LiPF_6 . The peaks of LiP_xF_y and $\text{LiP}_x\text{F}_y\text{O}_z$ can also be observed in P 2p spectra. The peak areas of the two compounds, along with LiF, as represented in [Supplementary Figure 2](#), indicate that the intensity of these compounds is greater in the case of Li anode cycled in the base electrolyte as compared to the LiDFOB-containing electrolyte. This provides further confirmation that the SEI film formed by LiDFOB is stable and robust enough to suppress severe electrolyte decomposition. Notably, the weak peak signal observed in the position range from 198 eV to 184 eV for the Li anode cycled in the base electrolyte can be attributed to the overlap between B 1s and P 2s XPS peak positions. Specifically, the peak signal in the base electrolyte primarily corresponds to the P 2s spectra of $\text{Li}_x\text{PF}_y\text{O}_z$ (192.1 eV) and Li_xPF_y (194.5 eV) species as detected in P 2p spectra. The electrode cycled in the LiDFOB-containing electrolyte displays additional peaks associated with B-F (193.1 eV) and B-O (191.1 eV) in P 2s/B 1s spectra, B-O eV in O 1s, and B-O-C (290.3 eV) in C 1s spectra^[52,73]. These results suggest that the reduction decomposition products of LiDFOB participate in the SEI formation process.

Protection of microstructure for Ni-rich cathode

To evaluate the compatibility of LiDFOB with Ni-rich cathodes, various concentrations of the LiDFOB additive were added to the base electrolyte and evaluated in Li||NCM85 batteries with the cut-off voltages of 4.3 V. As shown in [Supplementary Figure 4](#), Li||NCM85 batteries show improved capacity retention with the addition of LiDFOB additive, from 85.5% (utilizing the base electrolyte) to 91.9% (with 1 wt% LiDFOB-added electrolyte), 100% (with 2 wt% LiDFOB-added electrolyte), and 88.4% (with 3 wt% LiDFOB-added electrolyte). These results suggest that 2 wt% is the optimized content of LiDFOB for Li||NCM85 batteries. It can be noted from [Figure 3A](#) that the Li||NCM85 battery cycled in the 2 wt% LiDFOB-containing electrolyte demonstrates a notable initial CE of 85.7% and an average CE of 99.9% throughout the 6th cycle to the 200th cycle, surpassing those observed in the base electrolyte. These findings suggest that the CEI film derived from LiDFOB effectively mitigates interfacial parasitic reactions. Consequently, the capacity retention of the battery after 250 cycles is substantially higher at 90.9% compared to the base electrolyte at 64.6% [[Figure 3B](#), vs. the discharge capacity at the 3rd cycle]. Accordingly, by comparing the GITT curves of the battery after the first and 150 cycles, the corresponding overpotentials, and Li^+ diffusion coefficients (D_{Li^+}), the battery cycled in the base electrolyte exhibits a significantly increased overpotential, accompanied by a rapidly reduced D_{Li^+} [[Figure 3C](#) and [Supplementary Figure 5](#)]. This may be related to the increasing electrode polarization due to the continuous accumulation of electrolyte parasitic reaction products and the structural degradation of the NCM85 cathode^[64]. In contrast, the NCM85 electrodes maintained a lower overpotential and a higher D_{Li^+} during cycling with the addition of LiDFOB, which is attributed to the stable NCM85 interfacial structure in the presence of the LiDFOB-derived CEI film [[Figure 3D](#) and [Supplementary Figure 5](#)]. Moreover, we further investigated the effect of LiDFOB on the stability of the NCM85 interfacial structure by increasing the charge cut-off voltage to 4.6 V. As shown in [Figure 3E](#), the introduction of LiDFOB into the base electrolyte can achieve a remarkable enhancement in the electrochemical performance of NCM85 with capacity retention as high as 74% after 300 cycles. This comprehensive performance is comparable to the high-voltage Ni-rich cathodes that have been reported

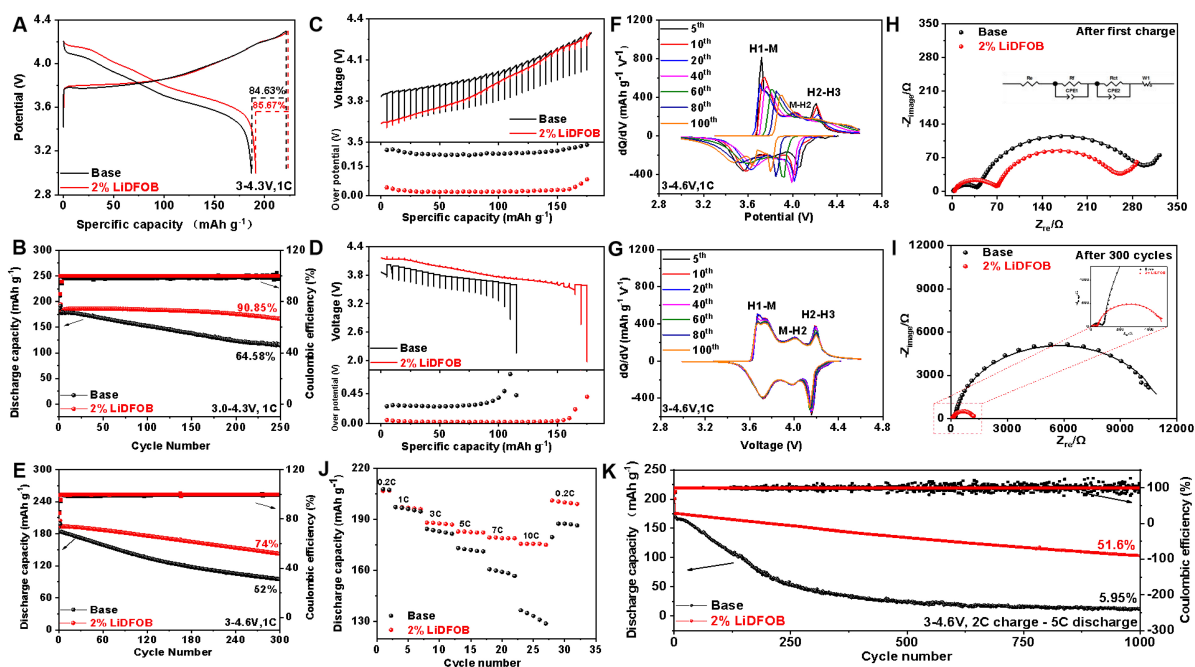


Figure 3. Electrochemical performance of the Li||NCM85 batteries with the base electrolyte and LiDFOB-containing electrolyte. (A) Typical voltage profiles of Li||NCM85 batteries with different electrolytes. (B) Cyclic stability of batteries at 1 C in the voltage range of 3.0–4.3 V at selected electrolytes. GITT curves and corresponding overpotential of (C) charging process and (D) discharging process after 150 cycles. (E) Cyclic stability of batteries at 1 C with a cut-off voltage of 4.6 V at selected electrolytes. The dQ/dV curves of Li||NCM85 batteries (F) without and (G) with 2 wt% LiDFOB additive. Nyquist plots for batteries (H) after the first cycle and (I) after 300 cycles, respectively. The inset is the enlarged view of the high-frequency area in the red dotted box of (I). (J) Rate capability of Li||NCM85 batteries in the voltage range of 3.0–4.6 V. (K) Cyclic stability and coulombic efficiency of Li||NCM85 batteries at the charge/discharge rate of 2 C/5 C in the voltage range of 3.0–4.6 V.

[Supplementary Table 2]. The corresponding charging/discharging profiles [Supplementary Figure 6] and dQ-dV profiles at different cycles [Figure 3F and G] demonstrate that the voltage drop and peak potential shift of the battery cycled with the LiDFOB-containing electrolyte are effectively mitigated. This observation further confirms that the CEI film derived from LiDFOB is robust and effectively protects the electrode from electrolyte erosion, even at high voltage.

Interfacial impedance was analyzed by EIS measurements to explore the interfacial evolution of the NCM85 electrode. The Nyquist plots of the battery mainly consist of two semicircles at high-to-medium frequency, corresponding to interfacial resistance (R_f) and charge transfer resistance (R_{ct}), while the slope of the line at low frequency provides the Warburg impedance (W_o) associated with the diffusion of Li^{+} [74,75]. The fitting results listed in Supplementary Table 3 were obtained via the equivalent circuit model (inset in Figure 3H). It is worth noting that both R_f and R_{ct} values obtained from the battery cycled with the base electrolyte exhibit a rapid increase, which can be attributed to the overgrowth of the interfacial film with high resistance that is formed due to electrolyte decomposition and the exacerbated structural degradation at the near-surface of the NCM85 crystal [Figure 3H]. In contrast, the NCM85 cathode cycled in the LiDFOB-containing electrolyte exhibits a less resistant interface and faster Li^{+} transport kinetics with the slow growth of R_f and R_{ct} [Figure 3I], indicating that the CEI film derived by LiDFOB can effectively mitigate the excessive decomposition of electrolyte and structural degradation at the near-surface of NCM85 crystal. The fast Li^{+} transport kinetics facilitates the rate performance of the battery. As shown in Figure 3J and K, the discharge capacity of the battery at 10 C increases significantly from 137 mAh g⁻¹ to 176 mAh g⁻¹ with the addition of LiDFOB. Besides, the battery cycled in the LiDFOB-containing electrolyte exhibits a high

capacity retention of 51.6% after 1,000 cycles at the charge/discharge rate of 2 C/5 C, compared with capacity retention of only 6% after 1,000 cycles in the base electrolyte with a more rapid capacity decay during the first 300 cycles.

More details about the evolution of structure were investigated by XRD (*in/ex-situ* XRD). The evolution of the (003) peak in *in-situ* XRD is related to the variation of the unit cell along the c-axis direction^[21,76]. It can be noted from the results of *in-situ* XRD [Figure 4A and B] that the interlayer spacing along the c-axis direction expands as Li⁺ is continuously extracted (with charging voltage ≤ 4.16 V) and responds by the shift of the (003) peak to a lower angle. When the charging potential is higher than 4.16 V, the sharp shift of the (003) peak to a high angle indicates a rapid contraction of the layer spacing along the c-axis, corresponding to the structural transformation from the H2 phase to the H3 phase, which leads to an increase in internal stress and structural degradation^[77]. For the battery cycled in the LiDFOB-containing electrolyte, the evolution angle of the (003) peak during the transition from the H2 phase to the H3 phase is observed to be lower than that in the base electrolyte [Figure 4A and B], especially when the current rate increases from the initial 0.1 C to 0.2 C in the second cycle (1.0774° vs. 1.1820°). This result indicates that the LiDFOB-derived CEI film is robust enough to mitigate the irreversible structural degradation of the cathode, which could be beneficial for improving the cycling stability of the battery. Similar conclusions can be drawn by testing the structural evolution before and after long cycles by *ex-situ* XRD [Supplementary Figure 7]. The variation range of the (003) peak in the base electrolyte (0.35°) after 300 cycles is larger than that in LiDFOB-containing electrolyte (0.28°), suggesting the superior structural reversibility of the NCM85 cathode cycled in the LiDFOB-containing electrolyte.

The phase transition process at high voltage is often accompanied by the oxidation of lattice oxygen to form O⁻^[78]. The high catalytic activity of O⁻ and the released oxygen will exacerbate the electrolyte decomposition, accompanied by the generation of CO₂^[79]. Therefore, the CO₂ content obtained by *in-situ* DEMS is used to monitor the gas evolution at the electrodes during cycling. It can be observed from Figure 4C that the battery cycled in the base electrolyte displays a sharply rising CO₂ signal when the charging cut-off voltage is higher than 4.5 V, suggesting the intensification of the lattice oxygen loss and electrolyte decomposition. In comparison, the CO₂ evolution in the LiDFOB-containing electrolyte is significantly suppressed, indicating that the introduction of LiDFOB can effectively stabilize lattice oxygen and suppress interfacial side reactions [Figure 4D].

The morphologies and interfacial components of the cycled NCM85 electrode in the base and LiDFOB-containing electrolytes were analyzed by the SEM (top-view and cross-section), TEM, and XPS, as shown in Figure 5. Compared with the fresh NCM85 electrode with an intact structure and clean and smooth surface [Figure 5A-C], severe interior cracks with partial crystal fragments can be observed on the particles after 200 cycles in the base electrolyte, and the electrode surface is also covered with an amorphous and inhomogeneous interfacial film with a thickness of about 30-60 nm [Figure 5D-F], which mainly results from the structural disruption of the NCM85 crystal and the deposition of electrolyte decomposition products. In contrast, the morphology of the NCM85 cathode cycled in LiDFOB-containing electrolyte is well maintained, and only a few cracks are discernible [Figure 5G and H]. Moreover, a relatively thin and uniform CEI film derived from the LiDFOB additive was observed to cover the surface of the NCM85, with a thickness of about 10 nm [Figure 5I], which can effectively protect the NCM85 electrode from electrolyte erosion and particle cracking. In C 1s spectra of the XPS spectra [Figure 5J], the peaks located at 290 eV, 288.5 eV, 286.5 eV, and 284.7 eV are assigned to the Li₂CO₃, C=O, C-O, and C-C species, respectively, which are mainly formed by the decomposition of organic solvent molecules (EC/EMC) in electrolyte^[80-82]. The deposits of C-O and C=O can also be observed at 533.4 eV and 531.8 eV in the O 1s spectra. The peaks

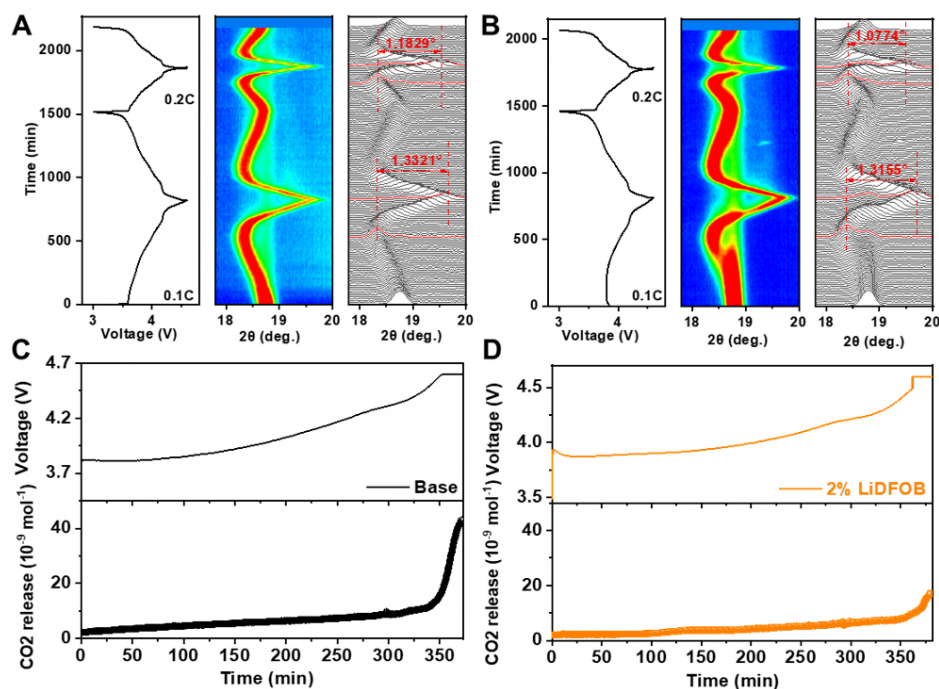


Figure 4. *In-situ* XRD patterns during the first two cycles of Li||NCM85 batteries (A) without and (B) with LiDFOB. DEMS test of Li||NCM85 batteries charging to 4.6 V in (C) the base electrolyte and (D) 2 wt% LiDFOB-containing electrolyte.

located at 685 eV and 686.8 eV in F 1s spectra are related to LiF and $\text{Li}_x\text{PO}_y\text{F}_z/\text{Li}_x\text{PF}_y$, arising from the decomposition of lithium salt (LiPF_6) in the electrolyte^[71,83]. The intensity of these peaks, represented by the peak area [Supplementary Figure 8], is significantly lower in the LiDFOB-containing electrolyte compared to the base electrolyte, providing evidence for the effective suppression of severe electrolyte decomposition by the application of LiDFOB additive. In addition, additional B-F (684.5 eV in F 1s spectra and 192.7 eV in B 1s spectra) and B-O peaks (190.5 eV in B 1s spectra)^[52,73] can only be observed in the LiDFOB-containing electrolyte, indicating the participation of LiDFOB in the construction of the protective CEI film. Furthermore, a peak signal was also detected in B 1s spectra on the NCM85 cathode surface cycled in the base electrolyte [Figure 5], similar to B 1s spectra observed on the Li anode surface [Figure 2G]. However, SEM and energy dispersive spectrometer (EDS)-mapping results [Supplementary Figure 9] clearly indicate a significantly higher amount of P element on the NCM85 cathode surface cycled in the base electrolyte, while the presence of B element is negligible. Therefore, the observed B 1s signal primarily arises from the overlap with the P 2s spectra peak positions. The robust signal intensity observed at the M-O (530.3 eV) peak in the LiDFOB-containing electrolyte, relative to the base electrolyte, provides evidence for the formation of a thinner and protective CEI film on the NCM85 electrode. This observation is consistent with the findings from TEM. In fact, the formation of a thinner CEI film has some advantages as it enables faster Li^+ transport in CEI film and reduced interfacial resistances compared to the progressively thickening deposits resulting from the decomposition of the base electrolyte. This conclusion is also supported by the results that the battery cycled in the LiDFOB-containing electrolyte exhibits significant improvement in rate performance than in the base electrolyte [Figure 3J and K].

Mechanism of the LiDFOB on SEI/CEI film formation

The possible redox decomposition pathways and the corresponding decomposition products of solvent (EC) and additive molecule (DFOB) were investigated by density functional theory (DFT) calculation. It shows that the preferential reduction of DFOB⁻ triggers the decomposition of EC on the anode side

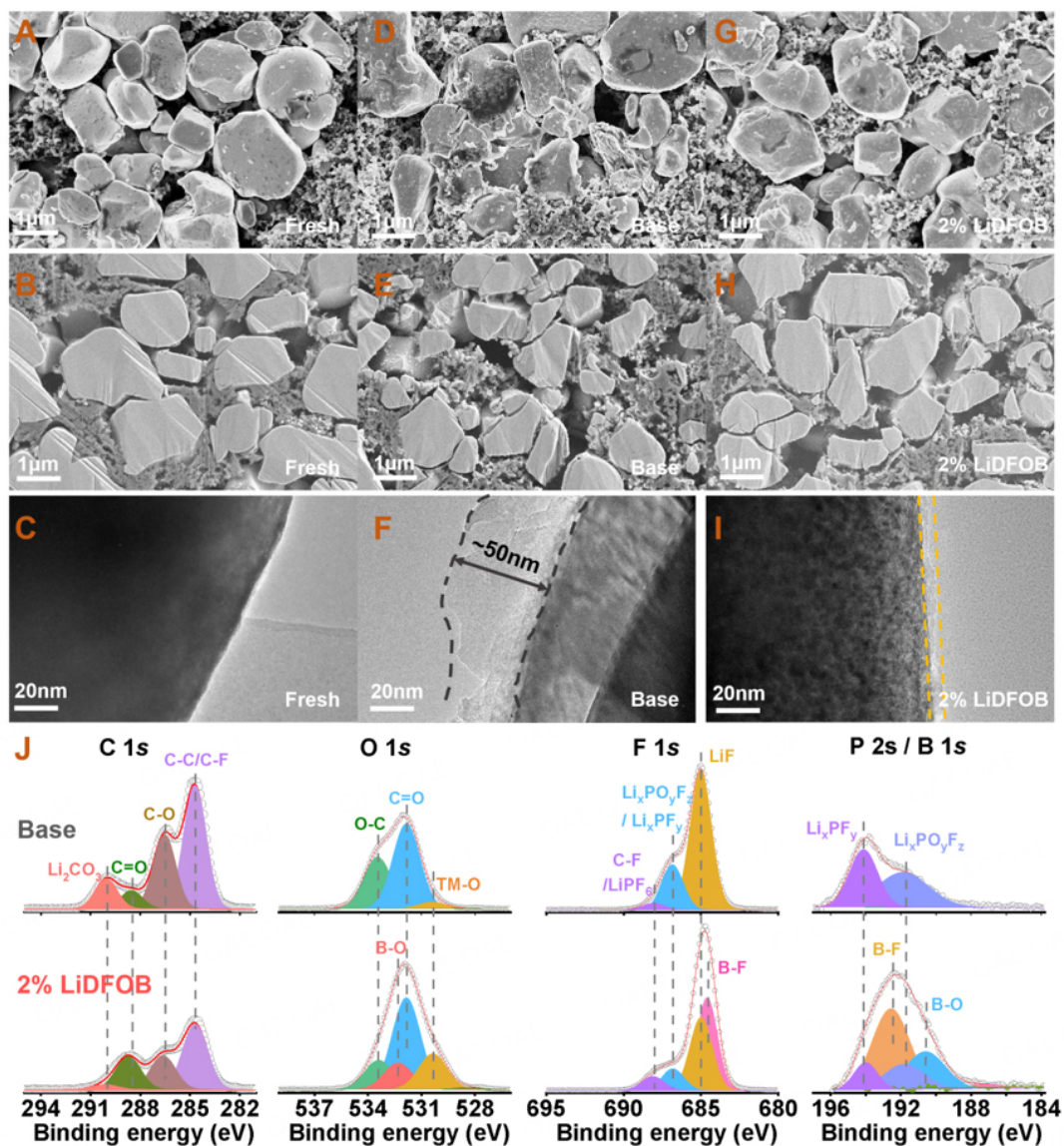


Figure 5. (A, D, G) Top-view, (B, E, H) cross-section SEM and (C, F, I) TEM images of (A-C) fresh and (D-I) cycled NCM85 electrodes after 200 cycles in the base and LiDFOB-containing electrolytes. (J) XPS spectra of C1s, O1s, F1s, and P 2s/B1s for the cycled NCM85 electrodes in the base and LiDFOB-containing electrolytes.

[Figure 6A]. Under the synergistic effect of the two, $\text{BF}_2\text{CH}_2\text{CH}_2\text{COOLi}$ and $\text{BF}_2\text{OCH}_2\text{CH}_2\text{CH}_2\text{CH}_2\text{OBF}_2$ polymers are formed, which are the main components of the SEI film, as confirmed by the B-O-C and B-F peaks detected in XPS [Figure 2G]. The reduction potentials of these polymers are comparable to those of the Li_2CO_3 , $\text{LiOOC}(\text{CH}_2)_4\text{COOLi}$, and $\text{CH}_3\text{CH}_2\text{OLi}$ products generated by the reduction decomposition of EC in the base electrolyte [Supplementary Figures 10A and 11], all of which exhibit good electrochemical stability on Li anode. While the higher LUMO-HOMO energy gaps (6.55 eV and 8.73 eV, Supplementary Figure 12) of these B-containing polymers indicate that the SEI film derived from DFOB⁻ exhibits a higher degree of electronic insulation properties compared to the electrolyte decomposition deposits. This property is advantageous in suppressing the parasitic reactions between the Li anode and electrolyte during the Li plating/stripping processes. The adsorption energy [Figure 6B] of $\text{BF}_2\text{CH}_2\text{CH}_2\text{COOLi}$ and $\text{BF}_2\text{OCH}_2\text{CH}_2\text{CH}_2\text{CH}_2\text{OBF}_2$ on Li (100) surface are -1.46 eV and -0.59 eV,

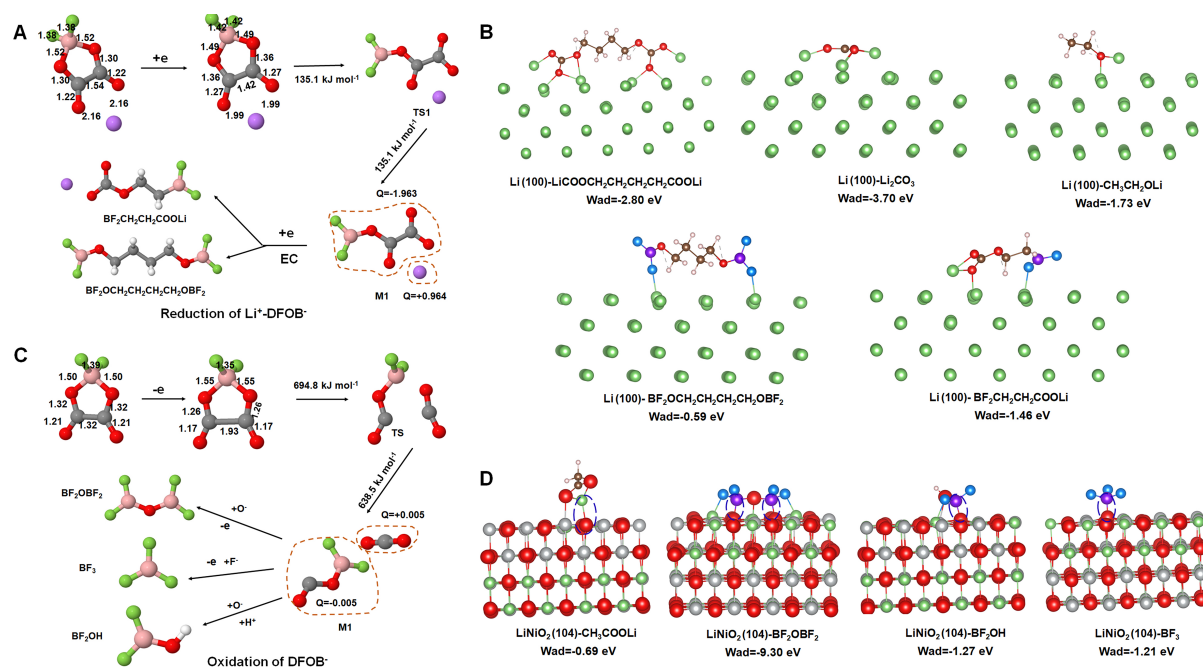


Figure 6. The formation mechanism of SEI and CEI films in LiDFOB-containing electrolyte by DFT calculation. (A) Reduction pathways of EC and $\text{Li}^+\text{-DFOB}^-$ and corresponding decomposition products on the anode side. (B) The adsorption energy of decomposition products on Li (100) surface. (C) Oxidation pathways of EC and DFOB^- and corresponding decomposition products on the cathode side, searched by DFT. (D) The adsorption energy of decomposition products on the LiNiO_2 (104) surface.

respectively, which are both lower than that of -3.7 eV, -2.8 eV, and -1.73 eV for $\text{Li}_2\text{CO}_3\text{-Li}$ (100), LEDC-Li (100), and $\text{CH}_3\text{CH}_2\text{OLi-Li}$ (100), suggesting a low bonding effect to Li, which can reduce the energy barrier associated with Li plating/stripping (as confirmed by the reduced nucleation overpotential in [Figure 2A](#)), thereby effectively facilitating the homogeneous plating/stripping of Li and enhances the electrochemical reversibility and cycling performance. For the NCM85 cathode, the EC molecules in the base electrolyte can be easily oxidized, forming CH_3COOLi and H^+ under the catalysis of O^- (formed from oxidation of the lattice oxygen) [[Supplementary Figure 10B](#)]. Furthermore, the formed HF will corrode the NCM85 cathode and further reduce the structural stability. With the introduction of the LiDFOB, the intermediates generated by its preferential oxidative decomposition can capture the harmful O^- , H^+ , and F^- , forming a BF_3 , BF_2OH , and BF_2OBF_2 -rich CEI film. These CEI film components have high antioxidant stability [[Figure 6C](#), [Supplementary Figure 13](#)] and electronic insulation [[Supplementary Figure 12](#)], which can effectively suppress the decomposition of electrolytes and the subsequent attack of HF to the NCM85 crystal. Moreover, the stronger adsorption energy of these B-containing compounds on the LiNiO_2 surface (-1.21 eV, -1.27 eV, and -9.3 eV for BF_3 , BF_2OH , and BF_2OBF_2 , respectively) compared to the -0.69 eV of $\text{CH}_3\text{COOLi-LiNiO}_2$ (104), indicates the B elements can form a strong bonding with the lattice oxygen on the NCM surface [[Figure 6D](#)], thus significantly mitigating the loss of lattice oxygen and degradation of the structural integrity of the cathode.

To further identify the composition and depth distribution of the SEI and CEI films, TOF-SIMS tests were performed for the Li anode [[Figure 7A and B](#)] and NCM85 cathodes [[Figure 7C and D](#)] after 20 cycles in the base and LiDFOB-containing electrolytes, respectively. The fragments of CH_2^- , LiO_2^- , and LiCO_3^- are mainly derived from the redox decomposition products of carbonate-based solvents in the electrolytes, such as lithium alkyl esters and Li_2CO_3 . The OH^- and LiF_2^- and NiF_2^- fragments are by-products of the decomposition of the electrolyte or the corrosion of the electrodes by HF, respectively. It can be noted from

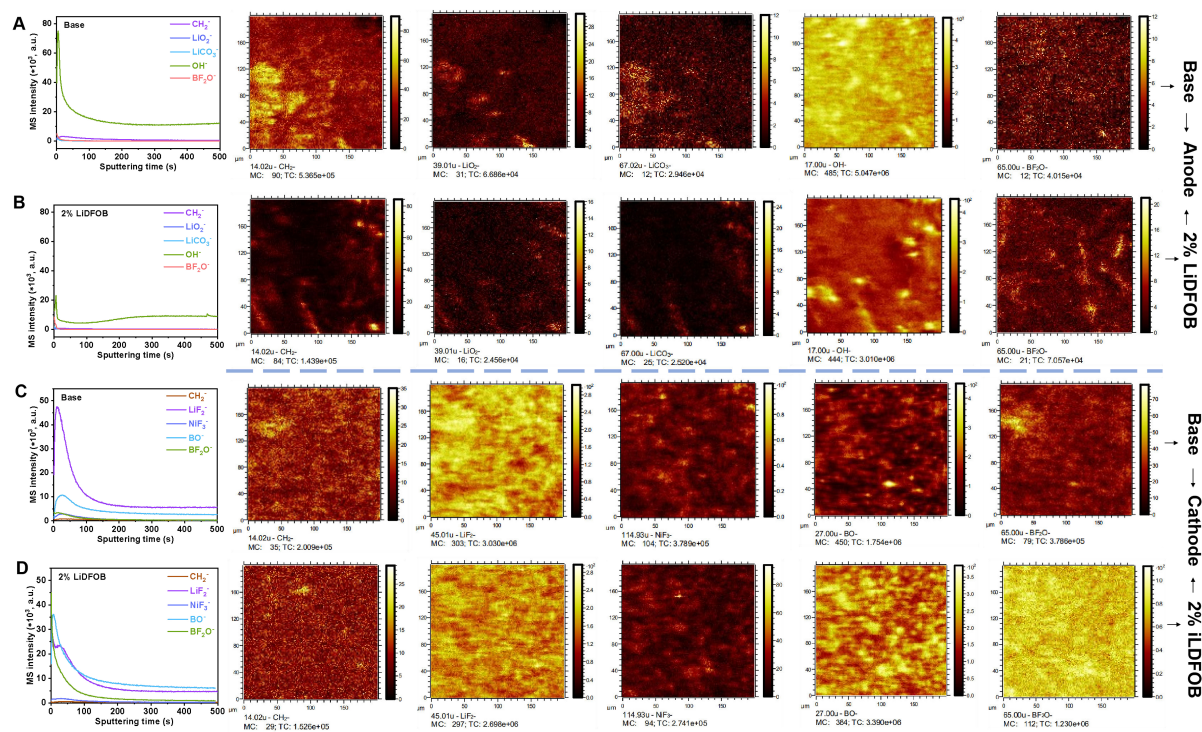


Figure 7. TOF-SIMS depth profiles and 2D mapping of (A and B) Li anodes and (C and D) NCM85 cathodes in different electrolytes.

the depth profiles [Figure 7A-D] that the intensity of these species on both electrodes cycled in the base electrolyte is higher than that in the LiDFOB-containing electrolyte, indicating that the introduction of LiDFOB can effectively suppress the decomposition of electrolytes and the corrosion of HF to both electrodes. In addition, compared to the electrodes cycled in the base electrolyte, the electrodes cycled in LiDFOB-containing electrolyte show significantly enhanced BF_2O^+ fragment signals, suggesting that a stable and BF_2 -rich interfacial film (SEI/CEI film) is constructed with the participation of LiDFOB on both the Li anode and NCM85 cathode surface, which is consistent with the theoretical calculation and XPS results.

CONCLUSIONS

In this study, the combination of computational and experimental results provides a comprehensive understanding of the working mechanisms of LiDFOB on suppressing the decomposition of electrolyte and stabilizing electrode structure in high voltage Li||NCM85 batteries. Based on the experimental results, it is evident that LiDFOB exhibits preferential reduction and oxidation decomposition on the surfaces of both Li anode and NCM85 cathode, leading to the formation of B-O-C, B-F bonds-containing SEI film and B-O, B-F bonds-containing CEI film, respectively, which can effectively prevent the degradation of the electrodes and inhibit the electrolyte decomposition. Theoretical calculations further confirm that the LiDFOB can be preferentially reduced on the Li anode surface to form highly electronically insulating $\text{BF}_2\text{CH}_2\text{CH}_2\text{COOLi}$ and $\text{BF}_2\text{OCH}_2\text{CH}_2\text{CH}_2\text{OBF}_2$ -rich SEI film, which can effectively suppress the reaction of highly reactive lithium with electrolyte and the formation of inactive lithium with the help of synergistic effect of EC. On the NCM85 cathode, LiDFOB is oxidized preferentially to form a CEI film containing BF_3 , BF_2OH , and BF_2OBF_2 species with high antioxidant stability and electronic insulation, which effectively suppresses the undesirable electrolyte decomposition and erosion of acidic species on the NCM85 cathode. Furthermore, the B element in the B-containing compounds of the CEI film forms a strong bond with the lattice oxygen of the NCM85 surface, mitigating the loss of lattice oxygen and structural degradation of the cathode.

Benefitting from the multifunctional nature of the LiDFOB additive, the Li||Li symmetry cell can also stably cycle for up to 1000 h at a current density of 0.5 mA cm⁻² in the carbonate electrolyte. Moreover, the rate capability and cyclic stability of Li||NCM85 batteries are significantly improved, with a high capacity retention of 74% after 300 cycles, even at a high charge cut-off voltage of 4.6 V. Our in-depth understanding of the working mechanisms of LiDFOB is expected to play a strategic role in guiding the rational design of electrolyte systems for high-energy-density lithium metal batteries.

DECLARATIONS

Acknowledgments

The authors thank Ningbo Ronbay Technology Co., Ltd. for kindly supplying the cathode material.

Authors' contributions

Manuscript writing: Yang X, Huang Y

Manuscript revision: Gong Z, Yang Y

All authors have given approval to the final version of the manuscript.

Availability of data and materials

The data supporting our findings can be found in the [Supplementary Materials](#).

Financial support and sponsorship

This work was financially supported by the National Key R&D Program of China (Grant No. 2021YFB2401800) and the National Natural Science Foundation of China (Grant Nos. 21935009, 22261160570, 22032004, and 22279108).

Conflicts of interest

All authors declared that there are no conflicts of interest.

Ethical approval and consent to participate

Not applicable.

Consent for publication

Not applicable.

Copyright

© The Author(s) 2023.

REFERENCES

1. Li M, Wang C, Chen Z, Xu K, Lu J. New concepts in electrolytes. *Chem Rev* 2020;120:6783-819. [DOI](#)
2. Blomgren GE. The development and future of lithium ion batteries. *J Electrochem Soc* 2017;164:A5019. [DOI](#)
3. Kim T, Song W, Son D, Ono LK, Qi Y. Lithium-ion batteries: outlook on present, future, and hybridized technologies. *J Mater Chem A* 2019;7:2942-64. [DOI](#)
4. Li M, Lu J, Chen Z, Amine K. 30 years of lithium-ion batteries. *Adv Mater* 2018;30:e1800561. [DOI](#)
5. Scrosati B, Hassoun J, Sun Y. Lithium-ion batteries. A look into the future. *Energy Environ Sci* 2011;4:3287-95. [DOI](#)
6. Xie J, Lu YC. A retrospective on lithium-ion batteries. *Nat Commun* 2020;11:2499. [DOI](#) [PubMed](#) [PMC](#)
7. Choi JU, Voronina N, Sun Y, Myung S. Recent progress and perspective of advanced high-energy Co-less Ni-rich cathodes for Li-ion Batteries: yesterday, today, and tomorrow. *Adv Energy Mater* 2020;10:2002027. [DOI](#)
8. Jiang F, Yang S, Liu H, et al. Mechanism understanding for stripping electrochemistry of Li metal anode. *SusMat* 2021;1:506-36. [DOI](#)
9. Shi P, Zhang X, Shen X, Zhang R, Liu H, Zhang Q. A review of composite lithium metal anode for practical applications. *Adv Mater Technol* 2020;5:1900806. [DOI](#)
10. Liu H, Sun X, Cheng X, et al. Working principles of lithium metal anode in pouch cells. *Adv Energy Mater* 2022;12:2202518. [DOI](#)

11. Yin S, Deng W, Chen J, et al. Fundamental and solutions of microcrack in Ni-rich layered oxide cathode materials of lithium-ion batteries. *Nano Energy* 2021;83:105854. DOI
12. Yan P, Zheng J, Liu J, et al. Tailoring grain boundary structures and chemistry of Ni-rich layered cathodes for enhanced cycle stability of lithium-ion batteries. *Nat Energy* 2018;3:600-5. DOI
13. Gao Y, Wang X, Geng J, Liang F, Chen M, Zou Z. Research progress on the failure mechanisms and modifications of Ni-rich ternary layered oxide cathode materials for lithium-ion batteries. *J Electron Mater* 2023;52:72-95. DOI
14. de Biasi L, Schwarz B, Brezesinski T, Hartmann P, Janek J, Ehrenberg H. Chemical, structural, and electronic aspects of formation and degradation behavior on different length scales of Ni-rich NCM and Li-rich HE-NCM cathode materials in Li-ion Batteries. *Adv Mater* 2019;31:e1900985. DOI PubMed
15. Geldasa FT, Kebede MA, Shura MW, Hone FG. Identifying surface degradation, mechanical failure, and thermal instability phenomena of high energy density Ni-rich NCM cathode materials for lithium-ion batteries: a review. *RSC Adv* 2022;12:5891-909. DOI PubMed PMC
16. Li S, Yao Z, Zheng J, et al. Direct observation of defect-aided structural evolution in a nickel-rich layered cathode. *Angew Chem Int Ed* 2020;59:22092-9. DOI
17. Sun J, Cao X, Zhou H. Advanced single-crystal layered Ni-rich cathode materials for next-generation high-energy-density and long-life Li-ion batteries. *Phys Rev Mater* 2022;6:070201. DOI
18. Wang X, Ruan X, Du CF, Yu H. Developments in surface/interface engineering of Ni-rich layered cathode materials. *Chem Rec* 2022;22:e202200119. DOI PubMed
19. Niu C, Liu D, Lochala JA, et al. Balancing interfacial reactions to achieve long cycle life in high-energy lithium metal batteries. *Nat Energy* 2021;6:723-32. DOI
20. Yoon M, Dong Y, Hwang J, et al. Reactive boride infusion stabilizes Ni-rich cathodes for lithium-ion batteries. *Nat Energy* 2021;6:362-71. DOI
21. Ryu H, Park K, Yoon CS, Sun Y. Capacity fading of Ni-rich $\text{Li}[\text{Ni}_x\text{Co}_y\text{Mn}_{1-x-y}]\text{O}_2$ ($0.6 \leq x \leq 0.95$) cathodes for high-energy-density lithium-ion batteries: bulk or surface degradation? *Chem Mater* 2018;30:1155-63. DOI
22. Zhang C, Wan J, Li Y, et al. Restraining the polarization increase of Ni-rich and low-Co cathodes upon cycling by Al-doping. *J Mater Chem A* 2020;8:6893-901. DOI
23. Zhu Z, Yu D, Shi Z, et al. Gradient-morph LiCoO_2 single crystals with stabilized energy density above 3400 Wh L^{-1} . *Energy Environ Sci* 2020;13:1865-78. DOI
24. Wang Y, Zhang Q, Xue Z, et al. An in situ formed surface coating layer enabling LiCoO_2 with stable 4.6 V high-voltage cycle performances. *Adv Energy Mater* 2020;10:2001413. DOI
25. Wang X, Wu Q, Li S, et al. Lithium-aluminum-phosphate coating enables stable 4.6 V cycling performance of LiCoO_2 at room temperature and beyond. *Energy Stor Mater* 2021;37:67-76. DOI
26. Yang X, Wang C, Yan P, et al. Pushing lithium cobalt oxides to 4.7 V by lattice-matched interfacial engineering. *Energy Stor Mater* 2022;12:2200197. DOI
27. Wang L, Liu T, Wu T, Lu J. Strain-retardant coherent perovskite phase stabilized Ni-rich cathode. *Nature* 2022;611:61-7. DOI
28. Li J, Zhou Z, Luo Z, et al. Microcrack generation and modification of Ni-rich cathodes for Li-ion batteries: a review. *Sustain Mater Technol* 2021;29:e00305. DOI
29. Liang L, Zhang W, Zhao F, et al. Surface/interface structure degradation of Ni-Rich layered oxide cathodes toward lithium-ion batteries: fundamental mechanisms and remedying strategies. *Adv Mater Interfaces* 2020;7:1901749. DOI
30. Zhang C, Jiang W, He W, Wei W. Heteroepitaxial interface of layered cathode materials for lithium ion batteries. *Energy Stor Mater* 2021;37:161-89. DOI
31. Zhang J, Li Q, Ouyang C, et al. Trace doping of multiple elements enables stable battery cycling of LiCoO_2 at 4.6 V. *Nat Energy* 2019;4:594-603. DOI
32. Zhu Z, Wang H, Li Y, et al. A surface Se-substituted $\text{LiCo}[\text{O}_{2.8}\text{Se}_8]$ cathode with ultrastable high-voltage cycling in pouch full-cells. *Adv Mater* 2020;32:e2005182. DOI
33. Wang L, Ma J, Wang C, et al. A novel bifunctional self-stabilized strategy enabling 4.6 V LiCoO_2 with excellent long-term cyclability and high-rate capability. *Adv Sci* 2019;6:1900355. DOI PubMed PMC
34. Jiang M, Danilov DL, Eichel R, Notten PHL. A review of degradation mechanisms and recent achievements for Ni-rich cathode-based Li-ion batteries. *Adv Energy Mater* 2021;11:2103005. DOI
35. Liu J, Wang J, Ni Y, Zhang K, Cheng F, Chen J. Recent breakthroughs and perspectives of high-energy layered oxide cathode materials for lithium ion batteries. *Mater Today* 2021;43:132-65. DOI
36. Ni L, Zhang S, Di A, et al. Challenges and strategies towards single-crystalline Ni-rich layered cathodes. *Adv Energy Mater* 2022;12:2201510. DOI
37. Wang X, Ding Y, Deng Y, Chen Z. Ni-rich/Co-poor layered cathode for automotive Li-ion batteries: promises and challenges. *Adv Energy Mater* 2020;10:1903864. DOI
38. Chen H, Pei A, Wan J, et al. Tortuosity effects in lithium-metal host anodes. *Joule* 2020;4:938-52. DOI
39. Liu W, Lin D, Pei A, Cui Y. Stabilizing lithium metal anodes by uniform Li-ion flux distribution in nanochannel confinement. *J Am Chem Soc* 2016;138:15443-50. DOI PubMed
40. Jie Y, Ren X, Cao R, Cai W, Jiao S. Advanced liquid electrolytes for rechargeable Li metal batteries. *Adv Funct Mater*

- 2020;30:1910777. DOI
41. Liu B, Zhang J, Xu W. Advancing lithium metal batteries. *Joule* 2018;2:833-45. DOI
 42. Zhang JG, Xu W, Xiao J, Cao X, Liu J. Lithium metal anodes with nonaqueous electrolytes. *Chem Rev* 2020;120:13312-48. DOI
 43. Yang X, Xu N, Liu G, et al. Modification and regulation of electrode/electrolyte interface for high specific energy and long life lithium ion batteries. *Chin Sci Bull* 2021;66:1170-86. DOI
 44. Zhao W, Ji Y, Zhang Z, et al. Recent advances in the research of functional electrolyte additives for lithium-ion batteries. *Curr Opin Electrochem* 2017;6:84-91. DOI
 45. Li L, Fu L, Li M, et al. B-doped and $\text{La}_4\text{NiLiO}_8$ -coated Ni-rich cathode with enhanced structural and interfacial stability for lithium-ion batteries. *J Energy Chem* 2022;71:588-94. DOI
 46. Birrozzi A, Laszczynski N, Hekmatfar M, von Zamory J, Giffin GA, Passerini S. Beneficial effect of propane sultone and tris(trimethylsilyl) borate as electrolyte additives on the cycling stability of the lithium rich nickel manganese cobalt (NMC) oxide. *J Power Sources* 2016;325:525-33. DOI
 47. Cha J, Han J, Hwang J, Cho J, Choi N. Mechanisms for electrochemical performance enhancement by the salt-type electrolyte additive, lithium difluoro(oxalato)borate, in high-voltage lithium-ion batteries. *J Power Sources* 2017;357:97-106. DOI
 48. Cheng F, Zhang X, Wei P, et al. Tailoring electrolyte enables high-voltage Ni-rich NCM cathode against aggressive cathode chemistries for Li-ion batteries. *Sci Bull* 2022;67:2225-34. DOI
 49. Cui Y, Liang X, Chai J, et al. High performance solid polymer electrolytes for rechargeable batteries: a self-catalyzed strategy toward facile synthesis. *Adv Sci* 2017;4:1700174. DOI PubMed PMC
 50. Ehteshami N, Ibing L, Stolz L, Winter M, Paillard E. Ethylene carbonate-free electrolytes for Li-ion battery: study of the solid electrolyte interphases formed on graphite anodes. *J Power Sources* 2020;451:227804. DOI
 51. Han J, Lee JB, Cha A, et al. Unsymmetrical fluorinated malonateborate as an amphoteric additive for high-energy-density lithium-ion batteries. *Energy Environ Sci* 2018;11:1552-62. DOI
 52. Hu M, Wei J, Xing L, Zhou Z. Effect of lithium difluoro(oxalato)borate (LiDFOB) additive on the performance of high-voltage lithium-ion batteries. *J Appl Electrochem* 2012;42:291-6. DOI
 53. Jurng S, Brown ZL, Kim J, Lucht BL. Effect of electrolyte on the nanostructure of the solid electrolyte interphase (SEI) and performance of lithium metal anodes. *Energy Environ Sci* 2018;11:2600-8. DOI
 54. Liu S, Zhang Q, Wang X, Xu M, Li W, Lucht BL. LiFSI and LiDFBOP dual-salt electrolyte reinforces the solid electrolyte interphase on a lithium metal anode. *ACS Appl Mater Interfaces* 2020;12:33719-28. DOI
 55. Xia L, Lee S, Jiang Y, Xia Y, Chen GZ, Liu Z. Fluorinated electrolytes for Li-ion batteries: the lithium difluoro(oxalato)borate additive for stabilizing the solid electrolyte interphase. *ACS Omega* 2017;2:8741-50. DOI PubMed PMC
 56. Ji Y, Li S, Zhong G, et al. Synergistic effects of suberonitrile-LiBOB binary additives on the electrochemical performance of high-voltage LiCoO_2 electrodes. *J Electrochem Soc* 2015;162:A7015. DOI
 57. Sun Y, Tao M, Zou Y, et al. 2,2,5,5-tetramethyl-2,5-disila-1-oxacyclopentane as a bifunctional electrolyte additive for Ni-rich ($\text{LiNi}_{0.9}\text{Co}_{0.05}\text{Mn}_{0.05}\text{O}_2$) cathode in Li-ion batteries. *J Power Sources* 2023;556:232411. DOI
 58. Zhang X, Liu G, Zhou K, et al. Enhancing cycle life of nickel-rich $\text{LiNi}_{0.9}\text{Co}_{0.05}\text{Mn}_{0.05}\text{O}_2$ via a highly fluorinated electrolyte additive-pentafluoropyridine. *Energy Mater* 2022;1:100005. DOI
 59. Zhao W, Zheng G, Lin M, et al. Toward a stable solid-electrolyte-interfaces on nickel-rich cathodes: LiPO_2F_2 salt-type additive and its working mechanism for $\text{LiNi}_{0.5}\text{Mn}_{0.25}\text{Co}_{0.25}\text{O}_2$ cathodes. *J Power Sources* 2018;380:149-57. DOI
 60. Zhao W, Zheng B, Liu H, et al. Toward a durable solid electrolyte film on the electrodes for Li-ion batteries with high performance. *Nano Energy* 2019;63:103815. DOI
 61. Zhang B, Wang L, Wang X, et al. Sustained releasing superoxo scavenger for tailoring the electrode-electrolyte interface on Li-rich cathode. *Energy Stor Mater* 2022;53:492-504. DOI
 62. Chen J, Peng Y, Yin Y, et al. High energy density Na-metal batteries enabled by a tailored carbonate-based electrolyte. *Energy Environ Sci* 2022;15:3360-8. DOI
 63. Mao M, Huang B, Li Q, Wang C, He Y, Kang F. In-situ construction of hierarchical cathode electrolyte interphase for high performance $\text{LiNi}_{0.8}\text{Co}_{0.1}\text{Mn}_{0.1}\text{O}_2/\text{Li}$ metal battery. *Nano Energy* 2020;78:105282. DOI
 64. Wang C, Li X, Zhao Y, et al. Manipulating interfacial nanostructure to achieve high-performance all-solid-state lithium-ion batteries. *Small Methods* 2019;3:1900261. DOI
 65. Zhou P, Xia Y, Hou WH, et al. Rationally designed fluorinated amide additive enables the stable operation of lithium metal batteries by regulating the interfacial chemistry. *Nano Lett* 2022;22:5936-43. DOI
 66. Adams BD, Zheng J, Ren X, Xu W, Zhang J. Accurate determination of coulombic efficiency for lithium metal anodes and lithium metal batteries. *Adv Energy Mater* 2018;8:1702097. DOI
 67. Hafner J. Ab-initio simulations of materials using VASP: density-functional theory and beyond. *J Comput Chem* 2008;29:2044-78. DOI PubMed
 68. Wu B, Liu Q, Mu D, et al. Suppression of lithium dendrite growth by introducing a low reduction potential complex cation in the electrolyte. *RSC Adv* 2016;6:51738-46. DOI
 69. Chen J, Xing L, Yang X, Liu X, Li T, Li W. Outstanding electrochemical performance of high-voltage $\text{LiNi}_{1/3}\text{Co}_{1/3}\text{Mn}_{1/3}\text{O}_2$ cathode achieved by application of LiPO_2F_2 electrolyte additive. *Electrochim Acta* 2018;290:568-76. DOI
 70. Cao Z, Zheng X, Qu Q, Huang Y, Zheng H. Electrolyte design enabling a high-safety and high-performance Si anode with a tailored

- electrode-electrolyte interphase. *Adv Mater* 2021;33:e2103178. DOI
71. Li Q, Wang Y, Wang X, et al. Investigations on the fundamental process of cathode electrolyte interphase formation and evolution of high-voltage cathodes. *ACS Appl Mater Interfaces* 2020;12:2319-26. DOI
 72. Fan X, Ji X, Han F, et al. Fluorinated solid electrolyte interphase enables highly reversible solid-state Li metal battery. *Sci Adv* 2018;4:eaau9245. DOI PubMed PMC
 73. Parimalam BS, Lucht BL. Reduction reactions of electrolyte salts for lithium ion batteries: LiPF₆, LiBF₄, LiDFOB, LiBOB, and LiTFSI. *J Electrochem Soc* 2018;165:A251. DOI
 74. Yang X, Lin M, Zheng G, et al. Enabling stable high-voltage LiCoO₂ operation by using synergetic interfacial modification strategy. *Adv Funct Mater* 2020;30:2004664. DOI
 75. Yang X, Tang S, Zheng C, et al. From contaminated to highly lithiated interfaces: a versatile modification strategy for garnet solid electrolytes. *Adv Funct Mater* 2023;33:2209120. DOI
 76. Han Y, Jung SH, Kwak H, et al. Single- or poly-crystalline Ni-Rich layered cathode, sulfide or halide solid electrolyte: which will be the winners for all-solid-state batteries? *Adv Energy Mater* 2021;11:2100126. DOI
 77. Ryu H, Namkoong B, Kim J, Belharouak I, Yoon CS, Sun Y. Capacity fading mechanisms in Ni-Rich single-crystal NCM cathodes. *ACS Energy Lett* 2021;6:2726-34. DOI
 78. Yan P, Zheng J, Tang ZK, et al. Injection of oxygen vacancies in the bulk lattice of layered cathodes. *Nat Nanotechnol* 2019;14:602-8. DOI
 79. Zheng W, Shi C, Dai P, et al. A functional electrolyte additive enabling robust interphases in high-voltage LiLiNi_{0.8}Co_{0.1}Mn_{0.1}O₂ batteries at elevated temperatures. *J Mater Chem A* 2022;10:21912-22. DOI
 80. Ma Y, Chen K, Ma J, et al. A biomass based free radical scavenger binder endowing a compatible cathode interface for 5 V lithium-ion batteries. *Energy Environ Sci* 2019;12:273-80. DOI
 81. Dupin J, Gonbeau D, Vinatier P, Levasseur A. Systematic XPS studies of metal oxides, hydroxides and peroxides. *Phys Chem Chem Phys* 2000;2:1319-24. DOI
 82. Pereira-nabais C, Światowska J, Chagnes A, et al. Interphase chemistry of Si electrodes used as anodes in Li-ion batteries. *Appl Surf Sci* 2013;266:5-16. DOI
 83. Yang Y, Wang Y, Xue Z, et al. Meticulous guard: the role of Al/F doping in improving the electrochemical performance of high-voltage spinel cathode. *J Materiomics* 2021;7:585-92. DOI